Catalysis Today 357 (2020) 248–258

Contents lists available at ScienceDirect

Catalysis Today

journal homepage: www.elsevier.com/locate/cattod

Active sites for the oxygen reduction reaction in nitrogen-doped carbon nanofibers

Marthe E.M. Buan[a], Andrea Cognigni[a], John C. Walmsley[b], Navaneethan Muthuswamy[a], Magnus Rønning[a,*]

[a] Department of Chemical Engineering, Norwegian University of Science and Technology, 7491 Trondheim, Norway
[b] SINTEF Industry, Høgskoleringen 5, 7465 Trondheim, Norway

ARTICLE INFO

Keywords:
Oxygen reduction
Active site
Nitrogen-doped
Carbon nanofiber
Chemical vapor deposition
Expanded graphite

ABSTRACT

Understanding the role of iron and the nature of the active sites in nitrogen-doped carbon nanomaterials is vital for their future application as oxygen reduction electrocatalysts in fuel cells. In this paper, porphyrin-like Fe-N_4 sites have been identified in nitrogen-doped carbon nanofibers (N-CNFs) grown from iron nanoparticles by chemical vapor deposition (CVD). Acid treatment of the N-CNFs removed the iron growth particles and about 50% of the nitrogen groups from the pristine N-CNFs, without affecting the oxygen reduction performance. Performing electron energy loss spectroscopy (EELS) on the acid treated and annealed N-CNFs confirmed that the CVD synthesis method leads to iron being atomically incorporated into the N-CNF structure. Furthermore, X-ray absorption near-edge structure (XANES) analysis of the Fe *K*-edge indicates that the iron atoms are stabilized by four nitrogen atoms, reminiscent of the Fe-N_4 structure found in porphyrins. An evolution of the XANES spectrum was observed when performing the measurements under mildly reducing conditions, which was explained by oxygen being adsorbed on the Fe-N_4 sites at room temperature. The Fe-N_4 moieties embedded in the N-CNFs were resistant to acid leaching and the results suggest that these Fe-N_4 sites are active sites for the oxygen reduction in N-CNFs.

1. Introduction

High loadings of Pt are required on the cathode of proton exchange membrane (PEM) fuel cells to catalyze the slow oxygen reduction reaction (ORR). The low abundancy and high cost of the noble metal catalyst directly hinders the implementation and commercialization of PEM fuel cells. In this context, it is necessary to develop new catalysts for the ORR based on more inexpensive and abundant materials with similar catalytic activity and stability as Pt/C [1].

One of the most promising non-noble metal catalysts for the ORR in acidic electrolyte is carbon nanomaterials containing nitrogen and transition metals (Me-N-C). The first Me-N-C catalysts for the ORR were inspired by metallo-porphyrin complexes found in nature and consisted of transition metals coordinated to N_4-macrocycles [2–7]. Further improvement of the activity and stability of these catalysts was achieved by heat treatment of the metal N_4-macrocycles at high temperatures [4]. An important discovery was made in 1989, when Gupta et al. obtained an active ORR catalyst by pyrolyzing polyacrylonitrile (PAN) mixed with Co- or Fe-acetate instead of N_4-macrocycles [8]. This showed that electrocatalysts for the oxygen reduction could simply be prepared by the simultaneous presence of a metal precursor, a nitrogen precursor and a carbon precursor during the pyrolysis step. The discovery has led to many different synthesis methods and precursors being employed to synthesize N-doped carbon materials for the ORR [9,10].

It has recently been understood that the presence of even trace amounts of transition metals during the synthesis of N-doped carbon is important for achieving an active ORR catalyst in acidic electrolyte [11]. In addition, higher catalytic activity is usually observed for N-doped carbon catalysts prepared from Fe compared to their counterparts prepared from Co or Ni [12–16]. However, the role of iron and the nature of the active sites for the ORR in these N-doped carbon catalysts is still not clear [11,17–19]. While some groups argue that Fe simply facilitates the incorporation of nitrogen into the graphitic structure of carbon, creating nitrogen centered active sites (CN_x) [20–23], others claim that the active site consists of Fe centers stabilized by pyrrolic or pyridinic nitrogen (Fe-N_x) [24–30]. Some studies have also suggested that carbon encapsulated Fe or iron carbide particles can facilitate the oxygen reduction [31–33].

Nitrogen-doped carbon nanofibers (N-CNFs) and carbon nanotubes

* Corresponding author.
E-mail address: magnus.ronning@ntnu.no (M. Rønning).

https://doi.org/10.1016/j.cattod.2019.01.018
Received 6 September 2018; Received in revised form 10 December 2018; Accepted 3 January 2019
Available online 04 January 2019

(N-CNTs) prepared using Fe as growth catalyst have shown activity for the oxygen reduction reaction [12,14,16,34–36]. In several experimental studies X-ray photoelectron spectroscopy (XPS) analysis has indicated a correlation between the oxygen reduction current and the level of nitrogen doping in the N-CNF and N-CNT catalysts [37–39]. Especially pyridinic N has been widely recognized as the nitrogen functionality responsible for the catalytic activity due to delocalization of the π-electrons. Deconvolution of the N 1s region from XPS has indicated that the ORR activity of N-CNFs and N-CNTs increases as the presence of pyridinic N in the surface increases [34,40–42]. This apparent relation has also been explained by pyridinic N not being the active site for the ORR, but rather acting as a marker for edge plane exposure in N-doped carbon materials [43,44].

On the other hand, X-ray absorption near edge structure (XANES) analysis of N-CNTs prepared from Fe precursors has shown that Fe-N_x species are likely to be present in the carbon structure [45,46]. This is in line with ^{57}Fe Mössbauer characterization of a N-CNT/N-G catalyst where two doublets in the spectrum were assigned to Fe-N_x and/or C-Fe-N_2 coordination sites [35]. The ORR activity of all these N-CNT catalysts was thus attributed to the presence of iron-nitrogen species. Furthermore, it has been proposed that O_2 may be chemisorbed on the Fe-N_x sites [46]. This conclusion was also reached for a Fe-N-C catalyst where the best theoretical fit of the XANES spectra consisted of oxygen adsorbed on the iron center of porphyrinic Fe-N_4 [28].

In this study acid treatment, XPS, EELS and XANES analysis have been combined to confirm that Fe-N_4 moieties similar to iron porphyrin sites in heme are incorporated into N-CNFs when grown from iron nanoparticles. Moreover, the XANES measurements are performed in an inert atmosphere under mild heat treatment to show that O_2 is likely to be adsorbed on the Fe-N_4 sites at normal temperature and pressure. Acid treatment of the as-prepared N-CNFs removed the iron growth particles and approximately 50% of the nitrogen groups initially present in the catalyst material. Since Fe-N_4 sites were still present in the N-CNFs after treatment, and the oxygen reduction activity remained intact, it is proposed that the Fe-N_4 moieties are active sites for the ORR on N-CNFs.

2. Experimental

2.1. Synthesis and post treatment

Nitrogen-doped carbon nanofibers supported on expanded graphite (EG) were prepared following the same method as described in previous reports [16,36]. In brief, the growth catalyst (1.0 g, 20 wt% Fe/EG) was loaded into the reactor and reduced in an H_2/Ar flow (40/160 ml/min, 5.0/5.0, AGA) while heating the furnace to 650 °C. Subsequently, N-CNFs were grown at 650 °C using a synthesis gas mixture of CO/NH_3/H_2 (150/6.5/20 ml/min, 3.7/3.6/5.0, AGA). The synthesis time was 41 h to achieve high N-CNF yields.

Acid treatment was done by refluxing the N-CNFs in concentrated HNO_3 (65%, Sigma-Aldrich) at 110 °C for 3 h. The acid treatment was repeated three times in order to remove all of the iron particles present in the sample. In between the treatments, the N-CNFs were washed with de-ionized (DI) water. After acid treatment the sample was thoroughly washed with DI-water, ethanol and acetone before being dried. The obtained sample was named “NCNF-HNO3”. Part of the NCNF-HNO3 sample was then loaded into a reactor and heat treated at 900 °C in an Ar atmosphere for 2 h to remove oxygen functional groups. The sample was denoted “NCNF-HNO3-900” after heat treatment.

2.2. Physicochemical characterization

The specific surface area of the N-CNFs was calculated by the Brunauer-Emmet-Teller (BET) method from N_2 adsorption measurements performed in a Micromeritics TriStar II 3020. X-ray diffraction (XRD) was used to characterize the phases of the iron particles present in the N-CNFs. A Bruker D8 Advance DaVinci X-ray diffractometer with a LynxEye™ detector and Cu Kα radiation (λ = 1.54 Å) was employed and measurements were done in the 2θ angular range 20°–80° using a fixed slit of 0.6 mm. The diffractograms were analyzed using the software DIFFRAC.EVA and the PDF-4+ database from ICDD. Temperature-programmed oxidation (TPO) was performed in a Netzsch STA 449C thermo-microbalance. The sample (5–10 mg) was loaded into the thermogravimetric (TG) instrument and heated from 40 °C to 900 °C at a rate of 10 °C/min under a flow of synthetic air (80 mL/min, 5.0, AGA).

Transmission electron microscopy (TEM) using a Jeol JEM-ARM200 F TEM equipped with a Gatan Quantum Energy Filter for Electron Energy Loss Spectroscopy (EELS) was employed to characterize the nanostructure and composition of the N-CNFs. TEM samples were prepared by dispersing N-CNFs in isopropanol by ultra-sonication. A drop of the dispersion was then deposited on a holey carbon film supported by a copper grid and dried at room temperature. EELS data was acquired in Scanning (S)TEM mode as spectrum images with the TEM operating at 200 kV and processed using the Gatan Digital Micrograph software. Power-law backgrounds were removed from the EELS spectra and the quantification was based on using Hartree Slater cross-sections.

X-ray photoelectron spectroscopy (XPS) measurements were carried out in a Kratos Axis Ultra DLD spectrometer using monochromatic Al Kα radiation (hν = 1486.58 eV). Sample preparation was done by covering carbon tape with an even layer of catalyst powder. Survey spectra were collected using fixed analyzer pass energies of 160 eV while the high-resolution spectra were collected at pass energies of 20 eV. Data analysis was performed using the CasaXPS software. The elemental composition was calculated after the subtraction of Shirley-type backgrounds for the high-resolution spectra. The N 1s and O 1s XPS peaks were deconvoluted using Gaussian-Lorentzian line shapes with 30% Lorentzian weighting.

The X-ray absorption spectroscopy (XAS) spectra were acquired at the Swiss-Norwegian beamlines (BM01B) at the European Synchrotron Radiation Facility (ESRF) in Grenoble, France. The samples were placed in a quartz capillary tube (2 mm outer diameter) and mounted in a sample holder connected to a He gas line. A vertical heat blower was placed underneath the capillary allowing for heating of the sample (0–400 °C). The setup configuration was similar to the one described and used by Tsakoumis et al. [47]. XAS spectra of the Fe *K*-edge (7112 eV) were acquired using a Vortex fluorescence detector. The absorption energy was calibrated using a Fe foil. Scans were first acquired at room temperature without gas flow and then with a He flow (2 mL/min). Next, the sample was heated at 5 °C/min to 100 °C and subsequently to 200 °C under a He flow. The Fe *K*-edge of reference samples including metallic iron (α-Fe), iron carbide (χ-Fe_5C_2) and iron oxides (Fe_2O_3, FeO) were measured at room temperature. The theoretical Fe *K*-edge XANES spectrum for iron porphyrin found in heme (denoted “Fe-Heme model”) was simulated using the finite difference method near-edge structure package FDMNES [48].

All XAS scans were subjected to background subtraction and normalization using the Athena program from the IFEFFIT software package [49]. Changes in the XANES profiles were investigated using difference spectra, $\Delta\mu(E)$. First, $\mu_2(E)$ was shifted so that shoulder A (see Figs. 6 and 8) overlapped with shoulder A of $\mu_1(E)$. The difference spectrum was then obtained using the following equation:

$$\Delta\mu(E) = \mu_2(E) - \mu_1(E) \quad (1)$$

2.3. Electrochemical characterization

The electrochemical characterization was conducted in a conventional three-electrode setup using a reversible hydrogen electrode (RHE) as reference electrode and a platinum wire as counter electrode. All potentials reported in this paper are given versus the RHE. The Pt

counter electrode was kept in a separate compartment and did not affect the ORR performance of the N-CNFs as confirmed by our previous study [16]. A rotating ring disk electrode (RRDE, disk: 5 mm ϕ, ring: Pt with 20% collection efficiency) was used as working electrode. The N-CNF catalysts were deposited on the glassy carbon disk electrode using the method described by Schmidt et al. [50]. The catalyst suspension was prepared by sonicating 3.0 mg of N-CNFs in a mixture of 500 µL Millipore H_2O, 200 µL ethanol (100%), 200 µL isopropanol and 100 µL of 0.5 wt% Nafion® (DuPont™ DE521, Ion Power,Inc) for one hour. About 16 µL of the suspension was placed on the glassy carbon disk and dried under a N_2 flow giving approximately 245 µg/cm^2 of N-CNF catalyst on the electrode surface. For comparison, a high loading of commercial Pt/C catalyst (20 wt% Pt on Vulcan XC-72R, E-TEK) was prepared by the same procedure giving a total of 245 µg/cm^2 20 wt% Pt/C or 49 µg/cm^2 Pt on the glassy carbon electrode.

Before performing the ORR, the electrolyte was saturated with Ar and the electrodes were cleaned using cyclic voltammetry between 1.2 V and 0 V at different scanning rates. The background current was then measured by linear sweep voltammetry (LSV) from 1.10 V to 0.01 V at 5 mVs^{-1} in the Ar-saturated electrolyte. Oxygen reduction experiments were carried out in O_2-saturated 0.5 M H_2SO_4 (95–97% H_2SO_4, Sigma Aldrich) at room temperature. The potential range of the ORR measurements was 1.10 V–0.01 V, the scan rate 5 mVs^{-1} and the rotational speed 1600 rpm. The third cathodic scan after background subtraction is reported for all catalysts. Onset potentials for the oxygen reduction (E_{ORR}) were determined by comparing the LSV curve obtained in Ar with the ORR measurement. The potential at which the ORR curve separates from the LSV curve in Ar and the oxygen reduction starts to take place is defined as the E_{ORR}.

In order to detect the amount of H_2O_2 produced on the working electrode during the ORR, a constant potential of 1.2 V vs. RHE was applied to the Pt ring electrode. The H_2O_2 yield was calculated from the ring current (I_R), the disk current (I_D) and the collection efficiency of the Pt ring (N) using the following equation [51]:

$$H_2O_2(\%) = 200 \times \frac{(I_R/N)}{(I_R/N) + I_D} \quad (2)$$

3. Results and discussion

3.1. Post-treatment

Nitrogen-doped carbon nanofibers (N-CNFs) were grown from iron nanoparticles by a chemical vapor deposition method. The synthesis yield, i.e. the mass of obtained N-CNFs per mass of Fe growth catalyst, was 6.5 g/g_{Fe}. TEM analysis, Fig. 1A, show iron particles present at the tip of the N-CNFs after synthesis and indicates a tip growth mechanism. Treatment with concentrated HNO_3 followed by annealing in an Ar atmosphere was employed to remove the iron growth particles and oxygen functional groups from the N-CNFs respectively. The acid treatment was repeated three times to ensure that all the iron particles present in the sample were removed. The acid treated N-CNF sample was termed “NCNF-HNO3”, while the heat-treated sample was named “NCNF-HNO3-900”. After all treatment, no discrete iron particles could be observed in the tip or inside the N-CNFs as shown in Fig. 1B. The image in Fig. 1B is a STEM image and iron nanoparticles should show strong contrast under the high angle annular dark field (HAADF) imaging conditions employed. In addition, high-resolution TEM and STEM imaging was performed and indicated that most of the iron particles were removed from the N-CNFs by the acid treatment.

X-ray diffraction and temperature programmed oxidation (TPO) measurements also suggest that all iron particles in the pristine N-CNFs are removed by acid treatment, see Fig. 2. The main peaks related to iron appear at 2θ values between 40–50° in XRD and are displayed in Fig. 2a. Before acid treatment the X-ray diffractogram of the N-CNFs shows that the phase of the iron particles is mainly Hägg carbide, χ-

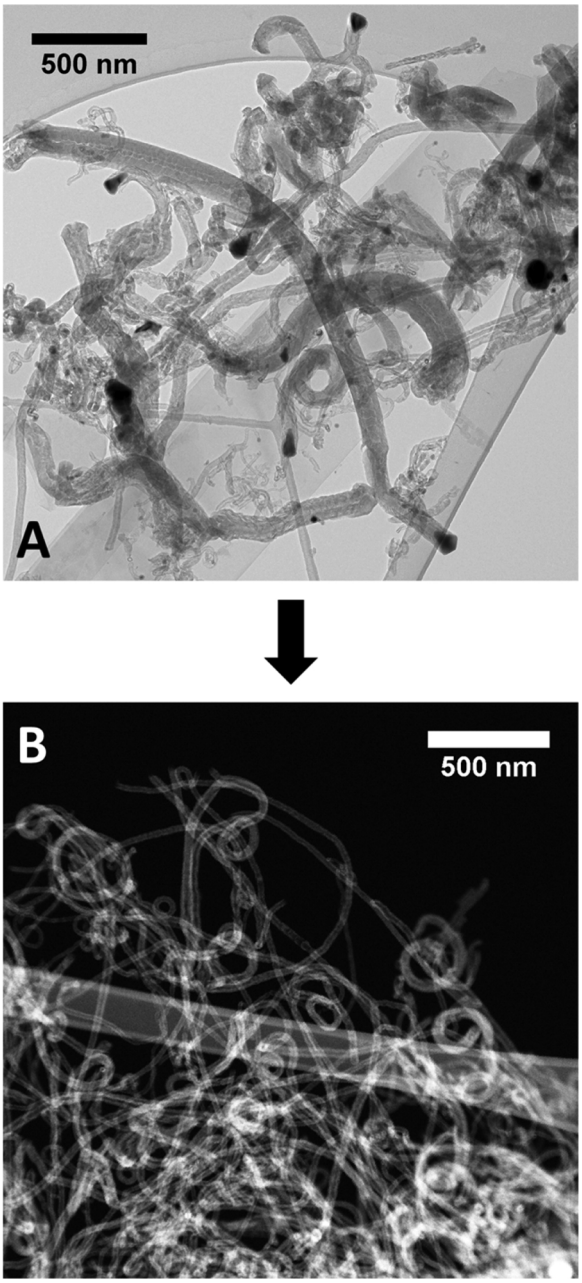

Fig. 1. A) TEM image of the pristine N-CNFs and **B**) STEM image of the N-CNFs after acid treatment and annealing.

Fe_5C_2 (PDF 04-014-4562), and not metallic iron. However, after acid treatment and annealing there was no signal from iron in XRD indicating that all crystalline iron had been removed from the N-CNFs.

Likewise, TPO of the N-CNFs before acid treatment showed 14% residual iron after the carbon had been removed by oxidation, while after acid treatment there were no detectable iron residues, see Fig. 2b. The oxidation temperature was not significantly altered by the acid treatment since the bulk oxidation temperature was 440 °C for NCNF and 460 °C for NCNF-HNO3. In addition, the oxidation of the expanded graphite support took place around 750 °C for both samples [16]. A weight loss at low temperatures was observed in the thermogravimetric curve only for NCNF-HNO3 and was due to the removal of oxygen functional groups in the surface introduced by the nitric acid.

Furthermore, removal of the iron growth particles was also confirmed by STEM/EELS analysis and XANES analysis of the acid treated and annealed N-CNFs, and will be discussed in more detail in

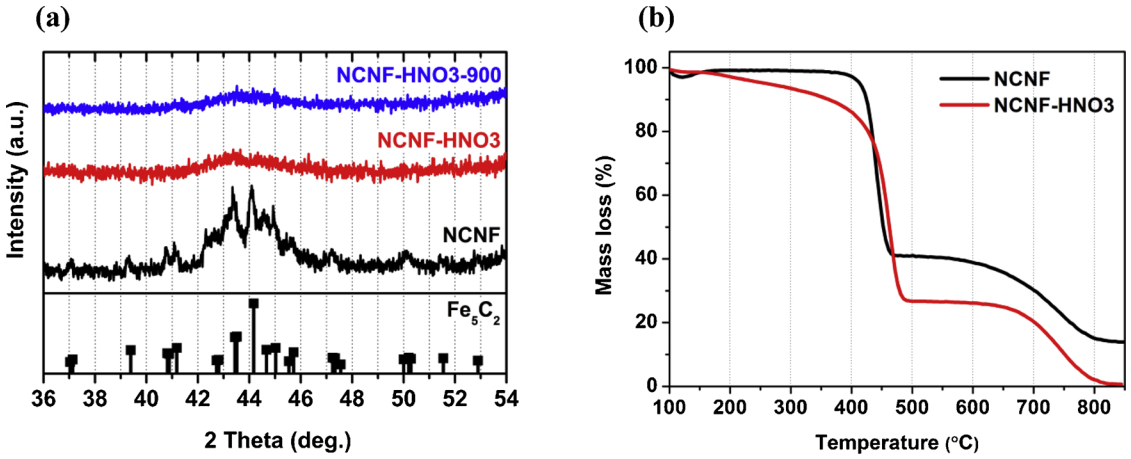

Fig. 2. (**a**) X-ray diffraction and (**b**) temperature programmed oxidation of the N-CNFs before and after acid treatment (and annealing).

succeeding chapters.

3.2. Oxygen reduction

The catalytic activity for the oxygen reduction reaction of N-CNFs before and after acid treatment and annealing was tested by performing linear sweep voltammetry in 0.5 M H_2SO_4, see Fig. 3. Before any treatment the N-CNFs showed an onset potential for the ORR, E_{ORR}, of 0.93 V and an oxygen reduction current of 0.63 mA/cm^2 at 0.7 V (Table 1). After refluxing in concentrated HNO_3 the catalytic activity for the ORR decreased slightly, while the amount of H_2O_2 detected decreased over the entire potential range. Nevertheless, the catalytic activity was completely restored or even slightly improved by annealing the NCNF-HNO3 in Ar, resulting in an ORR current of 0.68 mA/cm^2 at 0.7 V.

When comparing the N-CNF samples to a high loading of a commercial Pt catalyst (49 $\mu g_{Pt}/cm^2_{geo}$) it is clear that they are not in the same range. The Pt/C sample demonstrates a higher ORR performance in acidic electrolyte with an ORR onset potential of 1.05 V and a limiting current of 6.3 mA/cm^2. However, the main goal of this paper is to investigate the possible active sites present in N-CNFs prepared by CVD, rather than achieving a high ORR activity. In Fig. 3a, the N-CNFs are also compared with an undoped CNF sample containing the same iron carbide particles (χ-Fe_5C_2) as the N-CNF samples (confirmed by XRD in a previous paper [16]). The CNFs display a very low ORR activity, and consequently the presence of iron carbide particles will not contribute significantly to the ORR current of the N-CNFs. Doping of the CNF with nitrogen is thus crucial for forming ORR active sites, regardless of the active site structure being CN_x or Fe-N_x sites.

Cyclic voltammetry of the catalysts in Ar-saturated electrolyte showed that the electric double layer current increased with treatment. The slight increase in capacitive current for NCNF-HNO3-900 compared to the pristine N-CNFs could be due to the increase in specific surface area from 152 m^2/g for NCNFs to 210 m^2/g, see Table 1. Even though there are reports on carbon edges and defects improving the ORR performance of carbon materials, it is not likely that the change in surface area influenced the oxygen reduction activity of the N-CNFs. This is due to un-doped and metal-free carbon nanomaterials not being active for the ORR in acidic electrolyte, even with high surface area and porosity [52]. The N-CNFs treated with concentrated HNO_3 showed the highest double layer current which was related to the introduction of oxygen functional groups on the surface. In addition, a redox reaction was observed around 0.7 V for NCNF-HNO_3 and was attributed to the quinone to hydroquinone redox reaction (E° = 0.70 V). Since the ORR current and E_{ORR} decreased for the HNO_3-treated sample, it could seem that the presence of oxygen functional groups on the surface does not favor the ORR activity of N-CNFs.

3.3. X-ray photoelectron spectroscopy

X-ray photoelectron spectroscopy indicated the presence of iron, oxygen, nitrogen and carbon in the surface of all the samples and the elemental composition for the samples are presented in Table 1. In contrast to TEM, XRD and TPO measurements, a weak iron signal could still be detected in the acid treated and annealed N-CNFs by XPS analysis. As can be observed in Fig. 4, the iron signal decreased considerably after post-treatment and the iron content was estimated to decrease from 0.39 at% to 0.05-0.06 at%. The Fe $2p_{3/2}$ peak for the as-synthesized N-CNFs was broad and indicated contributions from both Fe^0 (707 eV) and iron oxides; Fe^{2+} (709.7 eV) / Fe^{3+} (711.2 eV). The presence of iron oxides was due to the surface of χ-Fe_5C_2 growth catalyst particles being partly oxidized [53]. After acid treatment the Fe signal was noisy and it was difficult to distinguish the features. Fitting of the Fe $2p_{3/2}$ peak for NCNF-HNO3 and NCNF-HNO3-900 with a single Gaussian peak indicated a shift to lower binding energy after annealing suggesting that the oxidation state of iron decreased slightly.

As expected, the treatment with HNO_3 introduced oxygen functional groups on the surface of the N-CNFs and increased the oxygen content from 1.9 at% to 5 at%. Before treatment the most pronounced oxygen group was found at 530 eV (O1) and originated from the presence of iron oxides. After acid treatment the amount of especially oxygen groups O2 and O3 increased considerably. In literature the O2 peak (531.1–531.3 eV) has been assigned to carbonyl oxygen groups in quinone [54], which is in agreement with the appearance of a peak at 0.7 V in the cyclic voltammetry curve (Fig. 3c). The assignment of oxygen peak O3 (532.4–532.5 eV) is subject to some debate, but is most likely due to COOH groups, or O=C−O groups in esters and anhydrides [55,56]. In any case, most of the oxygen groups were efficiently removed by annealing the NCNF-HNO3 at 900 °C in Ar resulting in an even lower total O-content for NCNF-HNO3-900 (1.2 at%) compared to pristine NCNF (1.9 at%).

Refluxing the N-CNFs with HNO_3 not only removed the iron particles and introduced oxygen functional groups, it also decreased the N-content drastically. The initial nitrogen content in the surface of the N-CNFs was 5.1 at%, but after acid treatment and annealing only 2.4 at% nitrogen was left in the fibers. In addition, the acid treatment altered the nitrogen groups present in the surface. Deconvolution of the high-resolution spectrum from the N 1 s region revealed that most of the nitrogen in the as-synthesized N-CNFs was incorporated as pyridinic N, N1 (398.4 eV), and quaternary N, N3 (401.1 eV). In addition, the deconvolution revealed the presence of four additional peaks located at 399.4 eV (N2), 402.6 eV (N4), 404.1 eV (N5) and 405 eV (N6) which were identified as amine (NH_2), pyridinic N-oxide, trapped N_2 gas and NO_2 groups respectively [36].

After HNO_3 treatment a clear peak appeared at 405.5 eV indicating

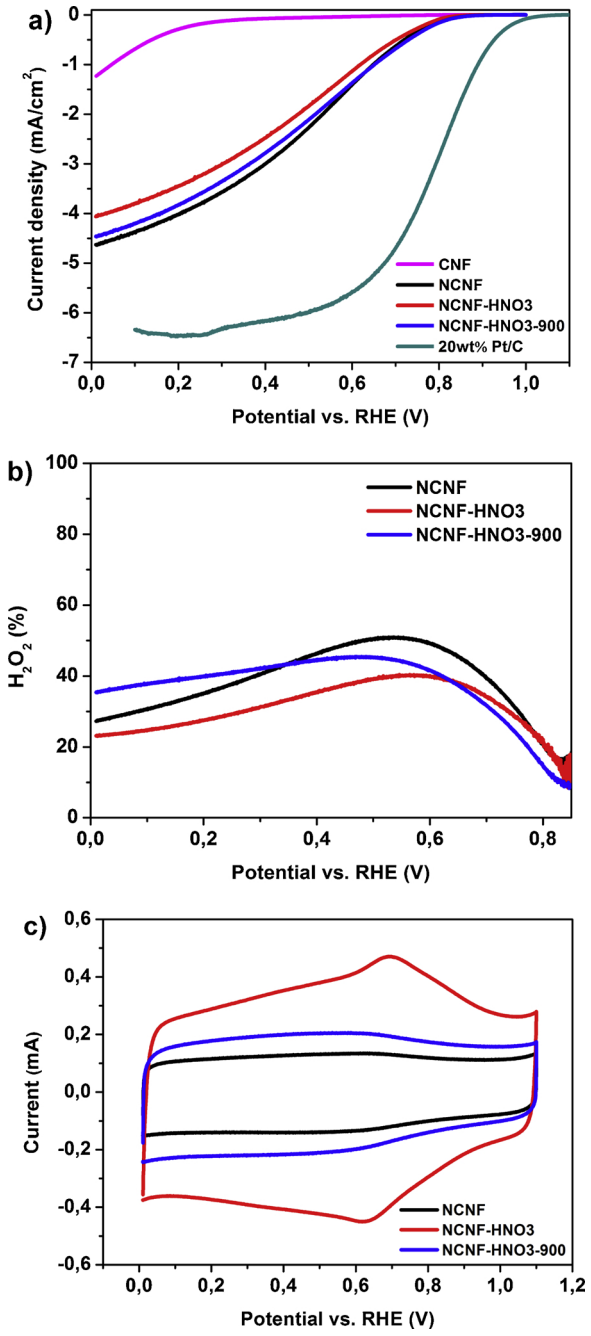

Fig. 3. (**a**) Oxygen reduction of the N-CNFs along with CNF and 20 wt% Pt/C references at 5 mV/s in 0.5 M H_2SO_4. (**b**) The corresponding amount of H_2O_2 detected on the Pt-ring for the N-CNF samples. (**c**) Cyclic voltammetry at 50 mV/s in Ar-saturated 0.5 M H_2SO_4. Conditions: 245 µg catalyst /cm^2, 1600 rpm.

the introduction of NO_2 groups from the acid. An additional peak next to the NO_2 peak had to be included in the deconvolution. It could therefore seem that the new peak N7 located at 407 eV was related to the NO_2 groups and not an individual contribution. Furthermore, the N2 peak which was identified as NH_2 groups shifted to a higher binding energy (399.8 eV) and increased in intensity. This could be attributed to the introduction of NO groups which have been reported to appear at binding energies around 400.1 eV [57,58]. The presence of carbonyl groups neighboring the NH_2 groups could also lead to a slight shift in the N2 peak position. Annealing the NCNF-HNO3 at 900 °C in Ar removed most of the oxygen functional groups introduced by the nitric acid. Furthermore, in the deconvolution of the N 1s region of NCNF-HNO3-900, Fig. 4b, the intensity of peak N2 and N6 decreased, while peak N7 was not present. This confirmed that these peaks were due to functional groups adsorbed on the N-CNF surface. The distribution of nitrogen groups was thus almost identical for the as-synthesized N-CNFs and the NCNF-HNO3-900 sample, even though the nitrogen content was 50% lower after treatment. It therefore appears that the amount of all the nitrogen groups decreased with treatment.

3.4. Electron energy loss spectroscopy

As stated above, TEM imaging of NCNF-HNO3-900 did not show any visible iron nanoparticles in the N-CNFs. However, XPS analysis indicated that there was still some iron left in the surface of the N-CNFs. Electron energy loss spectroscopy was therefore employed to identify the location of iron in the nanofibers. This technique is advantegeous over energy-dispersive X-ray spectroscopy (EDX) since it is not susceptible to secondary fluorescence effects by X-rays or scattered electrons. Fig. 5 displays the results from the EELS analysis of a representative N-CNF from the NCNF-HNO3-900 sample. The analysis area and the area selected to correct for sample drift are indicated in Fig. 5a, while the STEM image acquired during analysis is shown in Fig. 5b. Spectral images of the carbon *K*-edge and the nitrogen *K*-edge, Fig. 5c, correspond well with the inner structure of the carbon nanofiber and indicate that nitrogen is homogeneously doped into the N-CNFs. In contrast, the Fe *L*-edge was very weak and the spectral image is dominated by noise. As judged from the C *K*-edge map, the intensity of the Fe *L*-edge varied weakly with sample thickness suggesting that any Fe present is uniformly distributed in the analysis area.

The EELS spectrum from the red area in Fig. 5b was extracted and is shown in Fig. 5d. After background subtraction the edges of carbon, nitrogen and iron were clearly visible, see Fig. 5e-g. A number of N-CNFs were analyzed and a weak Fe signal was observed in all of them as shown in Fig. 5e for the bamboo-like N-CNF. Furthermore, Fe *L*-edge spectra from different locations within each carbon nanofiber were extracted and a weak signal was always detected. This indicates that iron is atomically incorporated into the N-CNFs as was also suggested from the spectral image of the Fe *L*-edge.

Tan et al. have described how the oxidation state of transition metal oxides correlates with their EELS spectra by using approaches such as edge onset values and white-line ratios [59]. The N-CNFs were studied using different spectrometer dispersions to maximize the sensitivity and resolution of the Fe *L*-edge peak structure from EELS. Furthermore, the spectra were compared with those obtained from Fe_2O_3 and metallic Fe reference materials. Unfortunately, it was not possible to reach a conclusion regarding the oxidation state of the Fe present in the N-CNFs by these methods here. This was partly due to the extremely weak Fe signal compared with those obtained from the reference materials.

The peak intensities of the different elements from EELS was

Table 1
Surface composition from XPS, specific surface area from N_2 adsorption measurements and oxygen reduction activity of the N-CNFs in 0.5 M H_2SO_4.

Sample	N *(at%)*	O *(at%)*	Fe *(at%)*	S_{BET} *(m^2/g)*	E_{ORR} *(V)*	E @ 1 mA/cm^2_{geo} *(V)*	j @ 0.7V *(mA/cm^2_{geo})*	H_2O_2 @ 0.7V *(%)*
NCNF	5.1	1.9	0.39	152	0.93	0.65	0.63	39.5
NCNF-HNO_3	2.8	5.0	0.05	199	0.91	0.62	0.51	34.1
NCNF-HNO_3-900	2.4	1.2	0.06	210	0.93	0.65	0.68	31.8

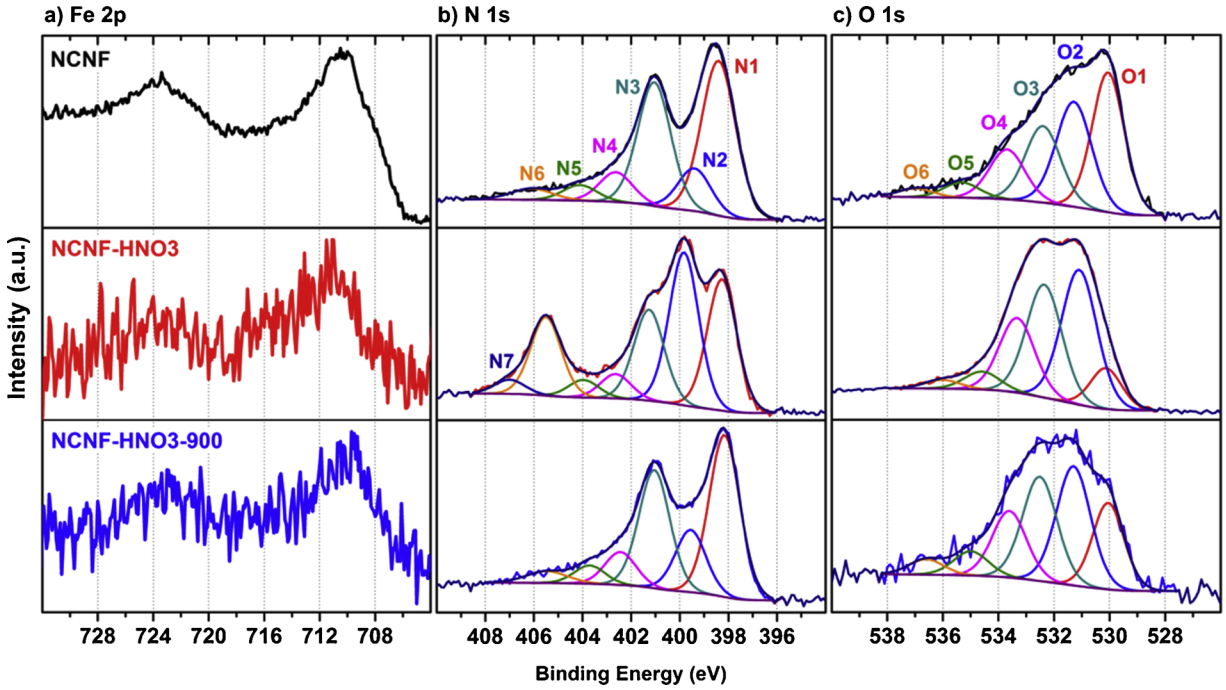

Fig. 4. High-resolution XPS spectra of the Fe 2p (**a**), N 1 s (**b**) and O 1 s (**b**) regions for NCNF (1st row), NCNF-HNO3 (2nd row) and NCNF-HNO3-900 (3rd row).

employed to estimate the bulk elemental composition of the N-CNFs. Quantification indicated N-doping levels of ~7 at% and Fe contents in the range of 0.4 at%. These values are significantly higher than the ones obtained from XPS quantification where the N and Fe contents were 2.4 at% and ~0.06 at% respectively (Table 1). This is expected since XPS is a surface sensitive technique and acid treatment would mainly remove nitrogen and iron species at the surface of the N-CNFs. The position of the *K*-edge of oxygen was also extracted from the EELS spectra in Fig. 5g, but it was weak and featureless. Quantification of oxygen therefore proved difficult as the oxygen signal was very sensitive to positioning of the peak and background subtraction levels. In general, the amount of oxygen in the N-CNFs was either very low or non-existent. As a result, the iron cannot be present as an oxide in the N-CNFs since this would have required a much stronger oxygen signal. In conclusion, the EELS analysis showed that growing N-CNFs from iron nanoparticles leads to the incorporation of iron atoms in the N-CNF structure.

3.5. X-ray absorption near-edge structure

X-ray absorption near edge structure (XANES) analysis at the Fe *K*-edge was used to gain information regarding the atomic structure of the iron incorporated in the N-CNFs. The XANES analysis was performed on the acid treated and annealed N-CNFs (NCNF-HNO3-900) since this sample did not contain iron carbide particles that would interfere with the analysis. A setup where the N-CNFs could be exposed to an inert atmosphere and mild heat treatment during XAS measurements was employed. This allowed for investigation on how possible adsorbed species would affect the XANES spectra. First, the NCNF-HNO3-900 sample was loaded into a quartz capillary and purged with helium at room temperature (20 °C) until the XANES of the Fe K-edge was stable. Fig. 6a displays the initial scan and the final scan, denoted "20 °C/He", which was obtained after exposing the N-CNFs to He for 1.5 h. It can be observed that the whole XANES spectrum, including the position of the absorption edge, shifts to lower energies when exposing the N-CNFs to He. In XANES analysis a decrease in the oxidation state of the absorption site usually results in a corresponding decrease in the absorption edge energy. It could therefore seem that adsorbed species such as O_2 or H_2O are being removed from the N-CNFs by the He flow, resulting in a lowering of the average oxidation state of Fe. However, this does not appear to affect the structure of the Fe-sites since the features of the XANES spectra did not change during He purging. By overlaying shoulder A at 7115 eV in the XANES of 20 °C/He with shoulder A for the initial scan, a difference spectrum, $\Delta\mu(E)$, was obtained. The $\Delta\mu$ spectrum is shown as an inset in Fig. 6a and demonstrates that there are no significant differences in the XANES features of the final scan compared to the initial scan. Thus, if desorption of weakly bonded species such as O_2 from the Fe centers in the N-CNFs is occurring, it results in a lowering of the average oxidation state of Fe without altering the surrounding environment.

A theoretical Fe *K*-edge XANES spectrum for the Fe site in iron porphyrin (Fe-N_4) was calculated using the FDMNES package and compared with the XANES spectrum of the NCNF-HNO3-900 sample. The structure of the modelled Fe-porphyrin was based on the core of the heme B group in hemoglobin where Fe is complexed to four pyrrolic nitrogen atoms as displayed in Fig. 6b. The computed XANES for the Fe-Heme model was similar to experimental XANES spectra obtained for different iron porphyrins by Xu et al. [60]. Comparing the NCNF-HNO3-900 XANES spectrum and its first derivative with the Fe-Heme model (Fig. 6b and c) shows that all the features A-E associated with the Fe-N_4 structure are present, despite differences in the relative intensity of some spectral features. The shoulder A appeared at 7115 eV in the N-CNF spectrum and can be assigned to the transition of 1 s core electrons to 3d states [61]. Furthermore, the presence of shoulder B at 7120 eV and peak C at 7132.5 eV are due to 1 s → 4p transitions characteristic of square-planar iron(II)-complexes such as Fe-N_4 in heme. Shoulder D (7138.5 eV) has been attributed to multiple scattering processes in similar Fe^{2+}-complexes and can according to Jia et al. show the local structure difference between Fe^{2+}-complexes with different Fe-N bond distances or spin states [61]. The experimental Fe *K*-edge XANES of NCNF-HNO3-900 also show the same features as reported by Zitolo et al. [28], Jia et al. [61] and Kramm et al. [62] for Fe-N-C catalysts containing high amounts of Fe-N_4 sites. It can therefore be concluded that most of the iron present in the N-CNFs after acid treatment and annealing originate from Fe-N_4 sites like the ones found in iron porphyrins.

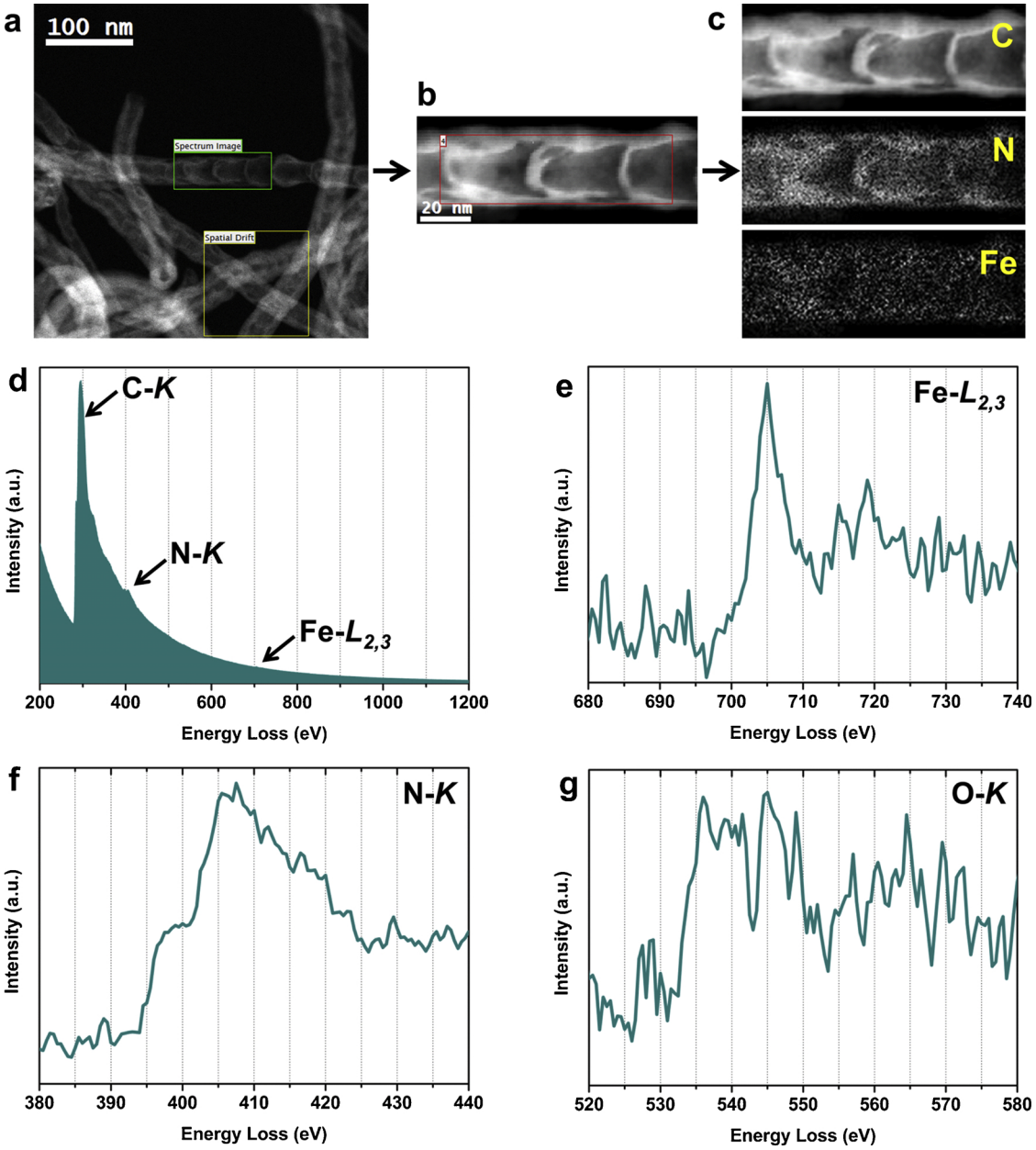

Fig. 5. (**a**) STEM and EELS analysis of acid treated and annealed N-CNFs with (**b**) HAADF image and (**c**) the corresponding EELS spectral images of C, N and Fe. (**d**) EELS spectrum from the red square in the HAADF image along with the (**e**) Fe $L_{2,3}$-edge, (**f**) N K-edge and (**g**) O K-edge (For interpretation of the references to colour in this figure legend, the reader is referred to the web version of this article).

Since the phase of the N-CNF growth catalyst particles was χ-Fe_5C_2 as confirmed by XRD, some trace amounts of iron carbide or iron oxide might remain in the N-CNFs after purification. This could affect the XANES spectrum and lead to differences in the absorption edge position and XANES features of NCNF-HNO3-900 compared to the Fe-Heme model. Therefore, Fe *K*-edge XANES spectra of metallic iron, iron carbides and iron oxides were also acquired. The experimental XANES spectra of χ-Fe_5C_2 and Fe_2O_3 are shown in Fig. 7 together with the stabilized spectrum of NCNF-HNO3-900 at 20 °C in He. In χ-Fe_5C_2 the Fe atoms are zero-valent, and the absorption edge is located at a lower photon energy compared to Fe_2O_3 where iron is present as Fe^{3+}. In comparison, the Fe absorption edge for the N-CNF sample is located at a slightly higher photon energy than Fe_2O_3 suggesting that the iron in the N-CNFs might also be present as Fe^{3+}. This edge position is consistent with the experimentally measured position of different iron porphyrins bonded with O or Cl atoms [60]. If significant amounts of χ-Fe_5C_2 or Fe_2O_3 had been present in the post-treated N-CNFs a lowering of the edge position should have been observed.

Furthermore, the features of the XANES spectra of χ-Fe_5C_2 and Fe_2O_3 are very different compared to the spectrum of NCNF-HNO3-900. Combining the experimentally measured XANES of χ-Fe_5C_2 and Fe_2O_3 with the theoretical XANES of the Fe-Heme model would therefore not yield a spectrum more similar to the one observed for the N-CNFs. This can be seen by comparing the first derivatives of all the spectra (Fig. 7b). A combination of the XANES of the Fe-Heme model with for example Fe_2O_3 would diminish shoulder B and feature C-D resulting in even larger differences between the Fe-Heme spectrum and the experimental NCNF-HNO3-900 spectrum. Thus, it was concluded that the iron carbide particles initially present in the N-CNFs were removed by the acid treatment, and are not affecting the XANES spectrum of NCNF-HNO3-900. Similar assessments were also performed for metallic iron and other iron carbides and iron oxides. The presence of none of these

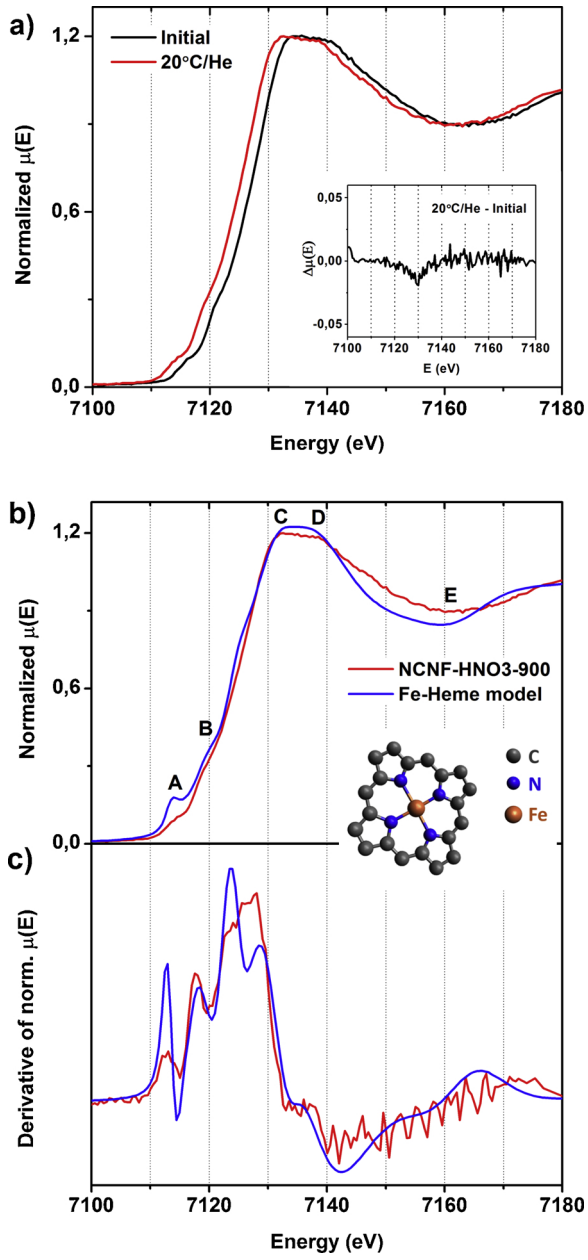

Fig. 6. (**a**) Normalized Fe K-edge XANES of NCNF-HNO3-900 collected at 20 °C in He, with the difference spectrum Δμ(E) between the stabilized and initial scan after aligning shoulder A (inset). (**b**) The stable spectrum of NCNF-HNO3-900 compared with a calculated XANES spectrum for the displayed Fe-Heme model and **(c)** the first derivative of the two spectra. The theoretical Fe-Heme spectrum was shifted 1.5 eV to higher energies to enable comparison of features A-E.

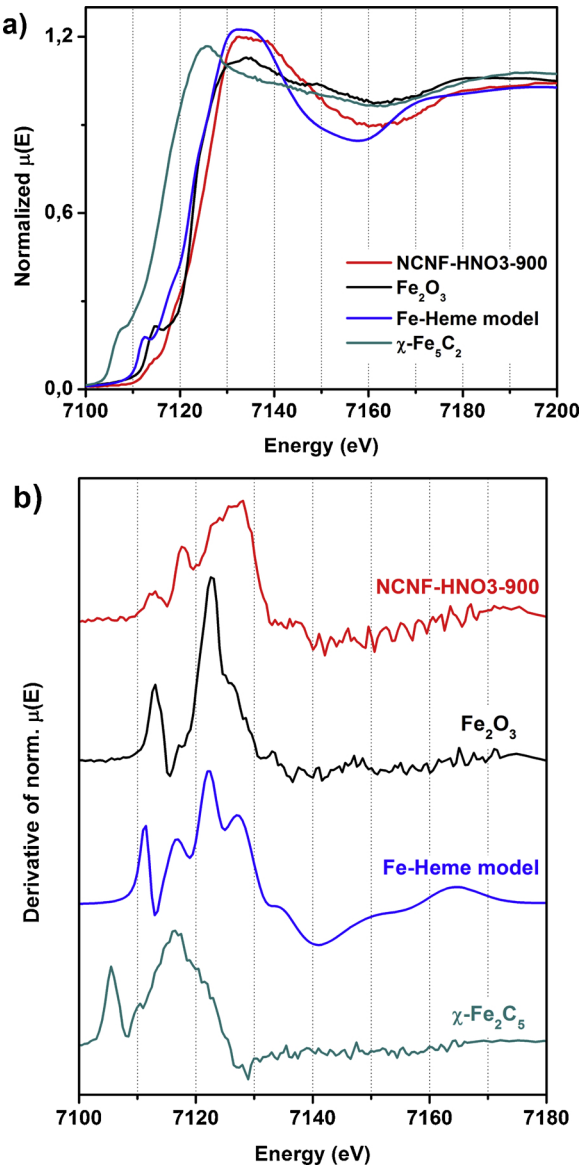

Fig. 7. (a) XANES at the Fe K-edge and **(b)** the corresponding first derivative for acid treated and annealed N-CNFs, the Fe-Heme model and experimental spectra for reference samples of iron oxide (Fe_2O_3) and Hägg carbide (χ-Fe_2C_5).

compounds could explain the slight discrepancies observed between the XANES of the Fe-Heme model and the acid treated and annealed N-CNFs. Most likely, the differences are instead related to the presence of several somewhat different Fe-N_4 sites in the N-CNFs, or just a consequence of the low loading and hence low signal-to-noise-ratio.

To investigate how the Fe *K*-edge XANES features of the post-treated N-CNFs evolved as more species were removed from the surface, the sample was heated in He atmosphere while acquiring XANES spectra. First NCNF-HNO3-900 was heated to 100 °C and kept for 5.5 h ("100 °C/He"), and then further heated to 200 °C and kept for another 5 h ("200 °C/He"), see Fig. 8. Heating at 100 °C in He shifted all the Fe *K*-edge features to slightly lower energies as was also observed when introducing He at room temperature. The $\Delta\mu(E)$ between spectrum 100 °C/He and 20 °C/He was obtained by overlaying shoulder A of the two spectra and is shown in Fig. 8b. The difference spectrum indicated that the shape of the main adsorption edge at 7124 eV and the white line were altered, while feature E slightly decreased. All these changes persisted and were even clearer when heating the acid treated N-CNFs at 200 °C in He, although shoulder A stayed at the same position as for 100 °C/He (7114.3 eV). When O_2 molecules are desorbed from Fe-N_4 sites in heme the Fe atom will eventually go from being in-plane oxygenated Fe^{3+}-N_4 to dome-shaped deoxygenated Fe^{2+}-N_4. This will alter the XANES features of the Fe *K*-edge and even small differences can be probed using $\Delta\mu(E)$ spectra. Recently Jia's research group modelled how this Fe^{3+} to Fe^{2+} phenomenon will affect the Fe *K*-edge XANES of Fe-N_4 sites and used this to explain changes in XANES features observed during in-situ oxygen reduction on their Fe-N-C catalysts [29,61]. The modelled and experimental changes in $\Delta\mu(E)$ for Fe-N_4 when removing oxygen and displacing the Fe atom out-of-plane included a shift in the adsorption edge to lower energies and a decrease in intensity of feature D and E [29]. All these changes are observed here when heating the NCNF-HNO3-900 under a He-flow, and the $\Delta\mu(E)$ spectra displayed in

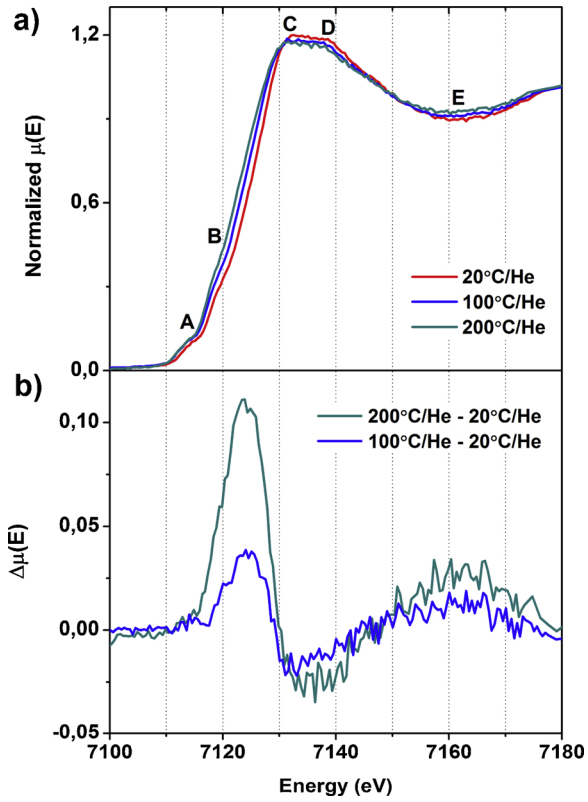

Fig. 8. (a) Fe K-edge XANES of NCNF-HNO3-900 during heating at different temperatures under He-flow. **(b)** Δμ(E) after aligning shoulder A for the XANES acquired at 100 °C and 200 °C with the stable XANES at room temperature (20 °C/He).

Fig. 8b show the same evolution as a response to more reducing conditions. (Note: here the *Δμ(E)* features are opposite since the oxygen rich state is used as reference, see Eq. 1). The results thus indicate that O_2 is being removed from the Fe-N_4 sites when exposing the N-CNF sample to He and heating. These observations support the hypothesis that O_2 from air will adsorb on Fe-N_4 sites at normal temperature and pressure (NTP) as previously suggested by Zhou et al. [46] and Zitolo et al. [28].

3.6. Active sites for the ORR

Nitrogen-doped carbon nanofibers prepared from or in the presence of iron usually exhibit higher catalytic activity for the oxygen reduction reaction compared to N-CNFs prepared from other transition metals [12–14,16]. However, the nature of the active sites for the ORR on N-CNFs is still unclear. Two main types of ORR active sites are usually debated: nitrogen-centered active sites (CN_x) and Fe-centered active sites (Fe-N_x). In addition, it has recently been suggested that carbon encapsulated Fe particles, iron carbide particles and carbon edges can facilitate the oxygen reduction [31–33,63,64].

Here, characterization with EELS and XANES confirmed that porphyrin-like Fe-N_4 sites are incorporated into N-CNFs grown from iron nanoparticles by chemical vapor deposition. The results indicate that the Fe-N_4 sites are resistant to acid leaching and atomically dispersed iron centers are still present in the N-CNFs after acid treatment and annealing. Porphyrin-like Fe-N_4 centers are known to be active for both oxygen adsorption and reduction. It is therefore likely that their presence will contribute to the catalytic activity of the N-CNFs. Active sites for the ORR consisting of Fe-N_4 would also explain why N-CNFs and N-CNTs prepared from Fe usually show higher catalytic activity than their counterparts prepared from Ni and Co [14,16].

Treatment with concentrated nitric acid removed both the iron growth catalyst particles and 50% of the nitrogen in the surface of the N-CNFs without affecting the ORR activity. This shows that the pristine N-CNFs contain substantial amounts of nitrogen and iron that are not contributing to the catalytic activity. According to XPS analysis, the two major N-groups in the N-CNFs were pyridinic N and quaternary N (Fig. 4). After acid washing and annealing, the ratio between the different nitrogen groups remained the same suggesting that the quantity of all the N-groups was reduced. Thus, if pyridinic or quaternary N-groups had been the main source of the ORR activity of the N-CNFs, a significant decrease in catalytic performance should have been observed after their removal. Instead, the ORR activity remained intact after treatment and it therefore seems likely that the presence of Fe-N_4 sites influences the ORR performance of the N-CNFs. This means that the correlation between N-content and ORR activity found in our previous study could simply indicate that the amount of Fe-N_4 sites increases as the total N-content of the N-CNFs increases [36]. Still, the study also found that the oxygen reduction on N-CNFs occurs through a sequential pathway. This enhances the possibility for several different active sites such as Fe-N_x and CN_x to collaboratively perform the ORR on the N-CNFs.

Several recent reports have concluded that the presence of iron carbide particles can improve the electrocatalytic activity of N-doped carbon nanomaterials [31,65,66]. This is however not the case for the N-CNFs in this study since an almost complete removal of the particles by refluxing in HNO_3 did not alter the ORR activity of the N-CNFs. In addition, undoped CNFs containing the same Hägg carbide particles (χ-Fe_5C_2) do not exhibit any ORR activity (Fig. 3a) [16], while a previous publication showed that KOH-treatment of N-CNFs reduced the presence of iron particles without significantly decreasing the ORR performance [67]. It is therefore clear that carbon encapsulated iron carbide nanoparticles are not contributing to the ORR performance of the N-CNFs prepared in this study. The presence of such iron carbide particles will instead make it harder to identify the Fe-N_4 sites by EELS and XANES analysis.

Carbon edges and defects have also been reported to enhance the ORR activity of nanocarbons [63,64]. Nevertheless, it is well-known that un-doped and metal-free carbon nanomaterials do not exhibit significant oxygen reduction currents in acidic electrolyte [52,68]. Thus, most publications on edge/surface effects of unmodified carbon materials only report the catalytic activity in alkaline electrolyte [69–71]. This means that even though the surface area and other surface properties of our N-CNFs was slightly altered by the acid treatment and annealing, there is no reason to believe this will significantly affect their ORR performance in acidic electrolyte.

In conclusion, this study confirms that porphyrin-like Fe-N_4 sites are incorporated into N-CNFs grown from iron nanoparticles. Based on the above discussion, we further propose that the Fe-N_4 moieties are active sites for the oxygen reduction in N-CNFs. It was also discovered that the Fe-N_4 structures are resistant to acid leaching and still present in the N-CNFs after acid treatment and annealing. However, the amount of Fe-N_4 moieties in N-CNFs is very low and difficult to detect using standard characterization techniques such as XRD, TPO, XPS and TEM. Masa et al. have suggested that nitrogen-doped carbon materials prepared using metal-containing precursors should be labeled Me-N-C catalysts, even after purification procedures [72]. This is in line with the results presented here as Fe-N_4 moieties are indeed present in N-CNFs grown from Fe, even after acid treatment. Our results highlight the importance of defining N-CNFs and N-CNTs prepared from metal-containing precursors as Me/N/C catalysts, even when they have been subjected to purification procedures. Possible contributions from Fe-N_x sites to the catalytic activity cannot be ruled out when using N-CNFs and N-CNTs prepared from Fe directly as catalysts or indirectly as catalyst supports.

4. Conclusion

Nitrogen-doped carbon nanofibers were grown on expanded

graphite from Fe nanoparticles using a chemical vapor deposition method. Characterization using XRD, TPO and TEM indicated that the iron particles were removed from the N-CNFs by thorough washing with nitric acid. However, a weak iron signal was still detected by EELS analysis of the acid treated and annealed N-CNFs with no visible iron particles, indicating that Fe is atomically incorporated into the N-CNF structure during growth. XANES measurements at the Fe *K*-edge revealed that the remaining iron in the N-CNFs was coordinated to nitrogen forming Fe-N_4 sites similar to iron porphyrin sites in heme. The catalytic activity for the oxygen reduction reaction of the N-CNFs was not affected by the acid treatment, although 50% of the nitrogen groups present in the surface of the N-CNFs were removed. It is therefore proposed that the Fe-N_4 moieties are active sites for the oxygen reduction on N-CNFs in acidic electrolyte.

Acknowledgements

Financial support was provided by the Norwegian University of Science and Technology (NTNU), the European Commission 7th Framework Programme (FP7) through the FREECATS project (grant no. 280658) and the Research Council of Norway (RCN) through the SYNKNØYT program (grant no. 218406). The TEM work was carried out at the NORTEM Gemini Centre at NTNU and supported by the NORTEM project (grant no. 197405) within the INFRASTRUCTURE program of the RCN. Experimental support with the XAS measurements from Diego A. Peña (NTNU) and the project team at the Swiss-Norwegian Beamlines (SNBL) at ESRF are gratefully acknowledged.

References

[1] D. Bokach, S. ten Hoopen, N. Muthuswamy, M.E.M. Buan, M. Rønning, Nitrogen-doped carbon nanofiber catalyst for ORR in PEM fuel cell stack: performance, durability and market application aspects, Int. J. Hydrogen Energy 41 (2016) 17616–17630, https://doi.org/10.1016/j.ijhydene.2016.07.137.
[2] R. Jasinski, A new fuel cell cathode catalyst, Nature 201 (1964) 1212–1213, https://doi.org/10.1038/2011212a0.
[3] H. Alt, H. Binder, G. Sandstede, Mechanism of the electrocatalytic reduction of oxygen on metal chelates, J. Catal. 28 (1973) 8–19, https://doi.org/10.1016/0021-9517(73)90173-5.
[4] H. Jahnke, M. Schönborn, G. Zimmermann, Organic dyestuffs as catalysts for fuel cells, Top. Curr. Chem. 61 (1976) 133–181 (Accessed 1 February 2015), http://www.ncbi.nlm.nih.gov/pubmed/7032.
[5] V.S. Bagotzky, M.R. Tarasevich, K.A. Radyushkina, O.A. Levina, S.I. Andrusyova, Electrocatalysis of the oxygen reduction process on metal chelates in acid electrolyte, J. Power Sources 2 (1978) 233–240, https://doi.org/10.1016/0378-7753(78)85014-9.
[6] J.A.R. van Veen, C. Visser, Oxygen reduction on monomeric transition metal phthalocyanines in acid electrolyte, Electrochim. Acta 24 (1979) 921–928, https://doi.org/10.1016/0013-4686(79)87088-7.
[7] G. Gruenig, K. Wiesener, S. Gamburzev, I. Iliev, A. Kaisheva, Investigations of catalysts from the pyrolyzates of cobalt-containing and metal-free dibenzotetraazaannulenes on active carbon for oxygen electrodes in an acid medium, J. Electroanal. Chem. Interfacial Electrochem. 159 (1983) 155–162, https://doi.org/10.1016/S0022-0728(83)80321-0.
[8] S. Gupta, D. Tryk, I. Bae, W. Aldred, E. Yeager, Heat-treated polyacrylonitrile-based catalysts for oxygen electroreduction, J. Appl. Electrochem. 19 (1989) 19–27, https://doi.org/10.1007/BF01039385.
[9] C.W.B. Bezerra, L. Zhang, K. Lee, H. Liu, A.L.B. Marques, E.P. Marques, H. Wang, J. Zhang, A review of Fe–N/C and Co–N/C catalysts for the oxygen reduction reaction, Electrochim. Acta 53 (2008) 4937–4951, https://doi.org/10.1016/j.electacta.2008.02.012.
[10] Z. Chen, D. Higgins, A. Yu, L. Zhang, J. Zhang, A review on non-precious metal electrocatalysts for PEM fuel cells, Energy Environ. Sci. 4 (2011) 3167, https://doi.org/10.1039/c0ee00558d.
[11] J.-P. Dodelet, The controversial role of the metal in Fe- or Co-based electrocatalysts for the oxygen reduction reaction, in: Acid Medium, M. Shao (Eds.), Electrocatal. Fuel Cells A Non- Low- Platin. Approach, Springer-Verlag London, London, 2013pp. 271–338.
[12] P.H. Matter, E. Wang, M. Arias, E.J. Biddinger, U.S. Ozkan, Oxygen reduction reaction activity and surface properties of nanostructured nitrogen-containing carbon, J. Mol. Catal. A Chem. 264 (2007) 73–81, https://doi.org/10.1016/j.molcata.2006.09.008.
[13] Y. Tang, S.C. Burkert, Y. Zhao, W.A. Saidi, A. Star, The effect of metal catalyst on the electrocatalytic activity of nitrogen-doped carbon nanotubes, J. Phys. Chem. C. 117 (2013) 25213–25221, https://doi.org/10.1021/jp403033x.
[14] X. Wang, Q. Li, H. Pan, Y. Lin, Y. Ke, H. Sheng, M.T. Swihart, G. Wu, Size-controlled large-diameter and few-walled carbon nanotube catalysts for oxygen reduction, Nanoscale. 7 (2015) 20290–20298, https://doi.org/10.1039/C5NR05864C.
[15] S. Ratso, I. Kruusenberg, A. Sarapuu, M. Kook, P. Rauwel, R. Saar, J. Aruväli, K. Tammeveski, Electrocatalysis of oxygen reduction on iron- and cobalt-containing nitrogen-doped carbon nanotubes in acid media, Electrochim. Acta 218 (2016) 303–310, https://doi.org/10.1016/J.ELECTACTA.2016.09.119.
[16] M.E.M. Buan, N. Muthuswamy, J.C. Walmsley, D. Chen, M. Rønning, Nitrogen-doped carbon nanofibers on expanded graphite as oxygen reduction electrocatalysts, Carbon 101 (2016) 191–202, https://doi.org/10.1016/j.carbon.2016.01.081.
[17] G. Wu, K.L. More, C.M. Johnston, P. Zelenay, High-performance electrocatalysts for oxygen reduction derived from polyaniline, iron, and cobalt, Science 332 (2011) 443–447, https://doi.org/10.1126/science.1200832.
[18] M. Lefèvre, E. Proietti, F. Jaouen, J.-P. Dodelet, Iron-based catalysts with improved oxygen reduction activity in polymer electrolyte fuel cells, Science 324 (2009) 71–74, https://doi.org/10.1126/science.1170051.
[19] D. Singh, J. Tian, K. Mamtani, J. King, J.T. Miller, U.S. Ozkan, A comparison of N-containing carbon nanostructures (CNx) and N-coordinated iron–carbon catalysts (FeNC) for the oxygen reduction reaction in acidic media, J. Catal. 317 (2014) 30–43, https://doi.org/10.1016/j.jcat.2014.05.025.
[20] P.H. Matter, E. Wang, J.-M.M.M. Millet, U.S. Ozkan, Characterization of the iron phase in CNx-based oxygen reduction reaction catalysts, J. Phys. Chem. C. 111 (2007) 1444–1450, https://doi.org/10.1021/jp0651236.
[21] G. Liu, X. Li, P. Ganesan, B.N. Popov, Development of non-precious metal oxygen-reduction catalysts for PEM fuel cells based on N-doped ordered porous carbon, Appl. Catal. B Environ. 93 (2009) 156–165, https://doi.org/10.1016/j.apcatb.2009.09.025.
[22] G. Liu, X. Li, J.-W. Lee, B.N. Popov, A review of the development of nitrogen-modified carbon-based catalysts for oxygen reduction at USC, Catal. Sci. Technol. 1 (2011) 207, https://doi.org/10.1039/c0cy00053a.
[23] K. Strickland, E. Miner, Q. Jia, U. Tylus, N. Ramaswamy, W. Liang, M.-T. Sougrati, F. Jaouen, S. Mukerjee, Highly active oxygen reduction non-platinum group metal electrocatalyst without direct metal-nitrogen coordination, Nat. Commun. 6 (2015) 7343, https://doi.org/10.1038/ncomms8343.
[24] U.I. Koslowski, I. Abs-Wurmbach, S. Fiechter, P. Bogdanoff, Nature of the catalytic centers of porphyrin-based electrocatalysts for the ORR: a correlation of kinetic current density with the site density of Fe − N 4 centers, J. Phys. Chem. C. 112 (2008) 15356–15366, https://doi.org/10.1021/jp802456e.
[25] M. Lefèvre, J.P. Dodelet, P. Bertrand, Molecular oxygen reduction in PEM fuel cell conditions: ToF-SIMS analysis of co-based electrocatalysts, J. Phys. Chem. B 109 (2005) 16718–16724, https://doi.org/10.1021/jp0529265.
[26] M. Ferrandon, A.J. Kropf, D.J. Myers, K. Artyushkova, U.I. Kramm, P. Bogdanoff, G. Wu, C.M. Johnston, P. Zelenay, Multitechnique characterization of a polyaniline–iron–carbon oxygen reduction catalyst, J. Phys. Chem. C. 116 (2012) 16001–16013, https://doi.org/10.1021/jp302396g.
[27] U.I. Kramm, J. Herranz, N. Larouche, T.M. Arruda, M. Lefèvre, F. Jaouen, P. Bogdanoff, S. Fiechter, I. Abs-Wurmbach, S. Mukerjee, J.-P. Dodelet, Structure of the catalytic sites in Fe/N/C-catalysts for O2-reduction in PEM fuel cells, Phys. Chem. Chem. Phys. 14 (2012) 11673–11688, https://doi.org/10.1039/c2cp41957b.
[28] A. Zitolo, V. Goellner, V. Armel, M.-T. Sougrati, T. Mineva, L. Stievano, E. Fonda, F. Jaouen, Identification of catalytic sites for oxygen reduction in iron- and nitrogen-doped graphene materials, Nat. Mater. 14 (2015) 937–942, https://doi.org/10.1038/nmat4367.
[29] J. Li, S. Ghoshal, W. Liang, M.-T. Sougrati, F. Jaouen, B. Halevi, S. McKinney, G. McCool, C. Ma, X. Yuan, Z.-F. Ma, S. Mukerjee, Q. Jia, Structural and mechanistic basis for the high activity of Fe–N–C catalysts toward oxygen reduction, Energy Environ. Sci. 9 (2016) 2418–2432, https://doi.org/10.1039/C6EE01160H.
[30] S. Ratso, N. Ranjbar Sahraie, M.T. Sougrati, M. Käärik, M. Kook, R. Saar, P. Paiste, Q. Jia, J. Leis, S. Mukerjee, F. Jaouen, K. Tammeveski, Synthesis of highly-active Fe–N–C catalysts for PEMFC with carbide-derived carbons, J. Mater. Chem. A 6 (2018) 14663–14674, https://doi.org/10.1039/C8TA02325E.
[31] Y. Hu, J.O. Jensen, W. Zhang, L.N. Cleemann, W. Xing, N.J. Bjerrum, Q. Li, Hollow spheres of iron carbide nanoparticles encased in graphitic layers as oxygen reduction catalysts, Angew. Chem. Int. Ed. 53 (2014) 3675–3679, https://doi.org/10.1002/anie.201400358.
[32] G. Zhong, H. Wang, H. Yu, F. Peng, Nitrogen doped carbon nanotubes with encapsulated ferric carbide as excellent electrocatalyst for oxygen reduction reaction in acid and alkaline media, J. Power Sources 286 (2015) 495–503, https://doi.org/10.1016/j.jpowsour.2015.04.021.
[33] J. Zhu, M. Xiao, C. Liu, J. Ge, J. St-Pierre, W. Xing, Growth mechanism and active site probing of Fe3C@N-doped carbon nanotubes/C catalysts: guidance for building highly efficient oxygen reduction electrocatalysts, J. Mater. Chem. A 3 (2015) 21451–21459, https://doi.org/10.1039/C5TA06181D.
[34] Z. Mo, S. Liao, Y. Zheng, Z. Fu, Preparation of nitrogen-doped carbon nanotube arrays and their catalysis towards cathodic oxygen reduction in acidic and alkaline media, Carbon 50 (2012) 2620–2627, https://doi.org/10.1016/j.carbon.2012.02.021.
[35] S. Zhang, H. Zhang, Q. Liu, S. Chen, Fe–N doped carbon nanotube/graphene composite: facile synthesis and superior electrocatalytic activity, J. Mater. Chem. A Mater. Energy Sustain. 1 (2013) 3302, https://doi.org/10.1039/c2ta01351g.
[36] M.E.M. Buan, N. Muthuswamy, J.C. Walmsley, D. Chen, M. Rønning, Nitrogen-doped carbon nanofibers for the oxygen reduction reaction: importance of Iron growth catalyst phase, ChemCatChem 9 (2017) 1663–1674, https://doi.org/10.1002/cctc.201601585.
[37] S. Maldonado, K.J. Stevenson, Influence of nitrogen doping on oxygen reduction

electrocatalysis at carbon nanofiber electrodes, J. Phys. Chem. B 109 (2005) 4707–4716, https://doi.org/10.1021/jp044442z.
[38] Z. Chen, D. Higgins, H. Tao, R.S. Hsu, Z. Chen, Highly active nitrogen-doped carbon nanotubes for oxygen reduction reaction in fuel cell applications, J. Phys. Chem. C. 113 (2009) 21008–21013, https://doi.org/10.1021/jp908067v.
[39] Z. Chen, D. Higgins, Z. Chen, Nitrogen doped carbon nanotubes and their impact on the oxygen reduction reaction in fuel cells, Carbon 48 (2010) 3057–3065, https://doi.org/10.1016/j.carbon.2010.04.038.
[40] S. Kundu, T.C. Nagaiah, W. Xia, Y. Wang, S. Van Dommele, J.H. Bitter, M. Santa, G. Grundmeier, M. Bron, W. Schuhmann, M. Muhler, Electrocatalytic activity and stability of nitrogen-containing carbon nanotubes in the oxygen reduction reaction, J. Phys. Chem. C. 113 (2009) 14302–14310, https://doi.org/10.1021/jp811320d.
[41] C.V. Rao, C.R. Cabrera, Y. Ishikawa, In search of the active site in nitrogen-doped carbon nanotube electrodes for the oxygen reduction reaction, J. Phys. Chem. Lett. 1 (2010) 2622–2627, https://doi.org/10.1021/jz100971v.
[42] J.D. Wiggins-Camacho, K.J. Stevenson, Mechanistic discussion of the oxygen reduction reaction at nitrogen-doped carbon nanotubes, J. Phys. Chem. C. 115 (2011) 20002–20010, https://doi.org/10.1021/jp205336w.
[43] P.H. Matter, U.S. Ozkan, Non-metal catalysts for dioxygen reduction in an acidic electrolyte, Catal. Lett. 109 (2006) 115–123, https://doi.org/10.1007/s10562-006-0067-1.
[44] E.J. Biddinger, D. von Deak, U.S. Ozkan, Nitrogen-containing carbon nanostructures as oxygen-reduction catalysts, Top. Catal. 52 (2009) 1566–1574, https://doi.org/10.1007/s11244-009-9289-y.
[45] J. Yang, D.-J. Liu, N.N. Kariuki, L.X. Chen, Aligned carbon nanotubes with built-in FeN4 active sites for electrocatalytic reduction of oxygen, Chem. Commun. (2008) 329–331, https://doi.org/10.1039/B713096A.
[46] J. Zhou, P.N. Duchesne, Y. Hu, J. Wang, P. Zhang, Y. Li, T. Regier, H. Dai, Fe-N bonding in a carbon nanotube-graphene complex for oxygen reduction: an XAS study, Phys. Chem. Chem. Phys. 16 (2014) 15787–15791, https://doi.org/10.1039/c4cp01455c.
[47] N.E. Tsakoumis, A. Voronov, M. Rønning, W. van Beek, Ø. Borg, E. Rytter, A. Holmen, Fischer–Tropsch synthesis: An XAS/XRPD combined in situ study from catalyst activation to deactivation, J. Catal. 291 (2012) 138–148, https://doi.org/10.1016/j.jcat.2012.04.018.
[48] Y. Joly, X-ray absorption near-edge structure calculations beyond the muffin-tin approximation, Phys. Rev. B 63 (2001) 125120, https://doi.org/10.1103/PhysRevB.63.125120.
[49] B. Ravel, M. Newville, *ATHENA*, *ARTEMIS*, *HEPHAESTUS*: data analysis for X-ray absorption spectroscopy using *IFEFFIT*, J. Synchrotron Radiat. 12 (2005) 537–541, https://doi.org/10.1107/S0909049505012719.
[50] T.J. Schmidt, H.A. Gasteiger, G.D. Stäb, P.M. Urban, D.M. Kolb, R.J. Behm, Characterization of high-surface-area electrocatalysts using a rotating disk electrode configuration, J. Electrochem. Soc. 145 (1998) 2354–2358, https://doi.org/10.1149/1.1838642.
[51] U.A. Paulus, T.J. Schmidt, H.A. Gasteiger, R.J. Behm, Oxygen reduction on a high-surface area Pt/Vulcan carbon catalyst: a thin-film rotating ring-disk electrode study, J. Electroanal. Chem. 495 (2001) 134–145, https://doi.org/10.1016/S0022-0728(00)00407-1.
[52] K. Lehmann, O. Yurchenko, J. Melke, A. Fischer, G. Urban, High electrocatalytic activity of metal-free and non-doped hierarchical carbon nanowalls towards oxygen reduction reaction, Electrochim. Acta 269 (2018) 657–667, https://doi.org/10.1016/J.ELECTACTA.2018.03.054.
[53] C.S. Kuivila, J.B. Butt, P.C. Stair, Characterization of surface species on iron synthesis catalysts by X-ray photoelectron spectroscopy, Appl. Surf. Sci. 32 (1988) 99–121, https://doi.org/10.1016/0169-4332(88)90076-1.
[54] F. Vautard, H. Grappe, S. Ozcan, Stability of carbon fiber surface functionality at elevated temperatures and its influence on interfacial adhesion, Appl. Surf. Sci. 268 (2013) 61–72, https://doi.org/10.1016/j.apsusc.2012.11.158.
[55] W. Qi, W. Liu, B. Zhang, X. Gu, X. Guo, D. Su, Oxidative dehydrogenation on nanocarbon: identification and quantification of active sites by chemical titration, Angew. Chem. Int. Ed. 52 (2013) 14224–14228, https://doi.org/10.1002/anie.201306825.
[56] G. Wen, J. Diao, S. Wu, W. Yang, R. Schlögl, D.S. Su, Acid properties of nanocarbons and their application in oxidative dehydrogenation, ACS Catal. 5 (2015) 3600–3608, https://doi.org/10.1021/acscatal.5b00307.
[57] J.R. Pels, F. Kapteijn, J.A. Moulijn, Q. Zhu, K.M. Thomas, Evolution of nitrogen functionalities in carbonaceous materials during pyrolysis, Carbon 33 (1995) 1641–1653, https://doi.org/10.1016/0008-6223(95)00154-6.
[58] J.L. Hueso, J.P. Espinós, A. Caballero, J. Cotrino, A.R. González-Elipe, XPS investigation of the reaction of carbon with NO, O2, N2 and H2O plasmas, Carbon 45 (2007) 89–96, https://doi.org/10.1016/j.carbon.2006.07.021.
[59] H. Tan, J. Verbeeck, A. Abakumov, G. Van Tendeloo, Oxidation state and chemical shift investigation in transition metal oxides by EELS, Ultramicroscopy. 116 (2012) 24–33, https://doi.org/10.1016/j.ultramic.2012.03.002.
[60] W. Xu, K. Dziedzic-Kocurek, M. Yu, Z. Wu, A. Marcelli, C.R. Natoli, E. Paris, A. Marcelli, Spectroscopic study and electronic structure of prototypical iron porphyrins and their μ-oxo-dimer derivatives with different functional configurations, RSC Adv. 4 (2014) 46399–46406, https://doi.org/10.1039/C4RA04685D.
[61] Q. Jia, N. Ramaswamy, H. Hafiz, U. Tylus, K. Strickland, G. Wu, B. Barbiellini, A. Bansil, E.F. Holby, P. Zelenay, S. Mukerjee, Experimental observation of redox-induced Fe–N switching behavior as a determinant role for oxygen reduction activity, ACS Nano 9 (2015) 12496–12505, https://doi.org/10.1021/acsnano.5b05984.
[62] U.I. Kramm, I. Herrmann-Geppert, J. Behrends, K. Lips, S. Fiechter, P. Bogdanoff, On an easy way to prepare metal-nitrogen doped carbon with exclusive presence of MeN4-type sites active for the ORR, J. Am. Chem. Soc. 138 (2016) 635–640, https://doi.org/10.1021/jacs.5b11015.
[63] K. Waki, R.A. Wong, H.S. Oktaviano, T. Fujio, T. Nagai, K. Kimoto, K. Yamada, Non-nitrogen doped and non-metal oxygen reduction electrocatalysts based on carbon nanotubes: mechanism and origin of ORR activity, Energy Environ. Sci. 7 (2014) 1950, https://doi.org/10.1039/c3ee43743d.
[64] X. Zhao, X. Zou, X. Yan, C.L. Brown, Z. Chen, G. Zhu, X. Yao, Defect-driven oxygen reduction reaction (ORR) of carbon without any element doping, Inorg. Chem. Front. 3 (2016) 417–421, https://doi.org/10.1039/C5QI00236B.
[65] W.-J. Jiang, L. Gu, L. Li, Y. Zhang, X. Zhang, L.-J. Zhang, J.-Q. Wang, J.-S. Hu, Z. Wei, L.-J. Wan, Understanding the high activity of Fe-N-C electrocatalysts in oxygen reduction: Fe/Fe3C nanoparticles boost the activity of Fe-Nx, J. Am. Chem. Soc. 138 (2016) 3570–3578, https://doi.org/10.1021/jacs.6b00757.
[66] J.A. Varnell, E.C.M. Tse, C.E. Schulz, T.T. Fister, R.T. Haasch, J. Timoshenko, A.I. Frenkel, A.A. Gewirth, Identification of carbon-encapsulated iron nanoparticles as active species in non-precious metal oxygen reduction catalysts, Nat. Commun. 7 (2016) 1–9, https://doi.org/10.1038/ncomms12582.
[67] N. Muthuswamy, M.E.M. Buan, J.C. Walmsley, M. Rønning, Evaluation of ORR active sites in nitrogen-doped carbon nanofibers by KOH post treatment, Catal. Today 301 (2018) 11–16, https://doi.org/10.1016/j.cattod.2017.03.045.
[68] N. Alexeyeva, E. Shulga, V. Kisand, I. Kink, K. Tammeveski, Electroreduction of oxygen on nitrogen-doped carbon nanotube modified glassy carbon electrodes in acid and alkaline solutions, J. Electroanal. Chem. 648 (2010) 169–175, https://doi.org/10.1016/j.jelechem.2010.07.014.
[69] D. Liu, L. Tao, D. Yan, Y. Zou, S. Wang, Recent advances on non-precious metal porous carbon-based electrocatalysts for oxygen reduction reaction, ChemElectroChem 5 (2018) 1775–1785, https://doi.org/10.1002/celc.201800086.
[70] L. Tao, Q. Wang, S. Dou, Z. Ma, J. Huo, S. Wang, L. Dai, Edge-rich and dopant-free graphene as a highly efficient metal-free electrocatalyst for the oxygen reduction reaction, Chem. Commun. 52 (2016) 2764–2767, https://doi.org/10.1039/C5CC09173J.
[71] Y. Jiang, L. Yang, T. Sun, J. Zhao, Z. Lyu, O. Zhuo, X. Wang, Q. Wu, J. Ma, Z. Hu, Significant contribution of intrinsic carbon defects to oxygen reduction activity, ACS Catal. 5 (2015) 6707–6712, https://doi.org/10.1021/acscatal.5b01835.
[72] J. Masa, W. Xia, M. Muhler, W. Schuhmann, On the role of metals in nitrogen-doped carbon electrocatalysts for oxygen reduction, Angew. Chem. Int. Ed. 54 (2015) 10102–10120, https://doi.org/10.1002/anie.201500569.